Deep Inelastic Neutron Scattering in the Study of Atomic Momentum Distributions*

Alan C. Evans
Department of Physics, University of Warwick, Coventry CV4 7AL, U.K.

Jerry Mayers
Rutherford Appleton Laboratory, Chilton, Didcot, Oxfordshire OX11 0QX, U.K.

David N. Timms
Department of Physics and Physical Electronics, Portsmouth Polytechnic, King Henry I Street, Portsmouth PO1 2DZ, U.K.

Malcolm J. Cooper
Department of Physics, University of Warwick, Coventry CV4 7AL, U.K.

Z. Naturforsch. **48a**, 425–432 (1993); received December 3, 1991

The electron-volt spectrometer (EVS) at the pulsed neutron source facility (ISIS) is being developed for the study of atomic momentum distributions. Neutrons with energies in the range 1 to 100 eV are incident on the sample, and the time-of-flight (TOF) spectrum of the scattered beam is measured by an array of fixed detectors. A resonant foil difference technique is used to yield a set of TOF spectra for those neutrons scattered into a fixed energy and through fixed angles. Information on the momentum distribution of the target nuclei can be deduced within an impulse approximation in a procedure analogous to that in Compton scattering of electrons by photons.

Crystalline compounds containing aligned hydrogen bonds and other hydrogenous compounds are of particular interest owing to the high cross-section of the proton at these neutron energies. With improved statistical accuracy of the data it is anticipated that deviations of the proton's potential from a harmonic potential may be determined. Non-hydrogenous systems have also been investigated. A description is given of the basic theory and interpretive method. Data obtained on numerous systems are presented and discussed.

Key words: Compton profile; DINS; Neutron momentum.

1. Introduction

Deep Inelastic Neutron Scattering (DINS) is a recently developed technique for the study of nuclear momentum distributions. As with photon Compton scattering experiments [1], DINS measurements are performed within the Impulse Approximation (IA) [2], where it is assumed that the energy transferred to the target particle is significantly greater than its binding energy. The IA allows us to relate the neutron scattering function in a relatively simple way to the nuclear momentum distribution.

In the IA, the neutron scattering function $S(\boldsymbol{q}, \omega)$ is given by [3]

$$S(\boldsymbol{q}, \omega) = \int n(\boldsymbol{p})\, \delta\left[\omega - \frac{(\boldsymbol{p}+\boldsymbol{q})^2}{2M} + \frac{\boldsymbol{q}^2}{2M}\right] \mathrm{d}\boldsymbol{p}\,, \quad (1)$$

where $n(\boldsymbol{p})$ is the atomic momentum distribution, M the atomic mass, $\boldsymbol{q}$ the momentum transfer and ω the energy transfer (with $\hbar = 1$).

Taking the z-axis along $\boldsymbol{q}$, the above equation simplifies to

$$S(\boldsymbol{q}, \omega) = \frac{M}{q}\, J(y)\,, \quad (2)$$

where

$$y = \frac{M}{q}\left(\omega - \frac{q^2}{2M}\right) \quad (3)$$

and

$$J(y) = \int n(p_x, p_y, y)\, \mathrm{d}p_x\, \mathrm{d}p_y\,. \quad (4)$$

* Presented at the Sagamore X Conference on Charge, Spin and Momentum Densities, Konstanz, Fed. Rep. of Germany, September 1–7, 1991.

Current address of Dr. A. C. Evans is UG7, R3, Rutherford Appleton Laboratory, Chilton, Didcot, Oxfordshire OX11 0QX, U.K. Reprint requests to this address please.

0932-0784 / 93 / 0100-0425 $ 01.30/0. – Please order a reprint rather than making your own copy.

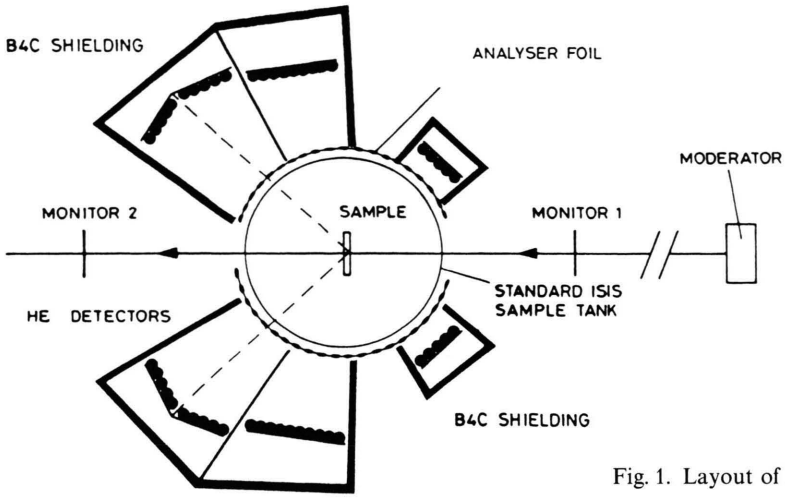

Fig. 1. Layout of EVS.

The results reported here were obtained using the pulsed neutron source at the ISIS facility, which is sited at the Rutherford Appleton Laboratory. The EVS spectrometer at ISIS can measure energy transfers in excess of 100 eV, therefore ensuring that corrections to the IA are small and making it a suitable instrument for these types of measurements.

2. The Electron Volt Spectrometer

A schematic diagram of the Electron Volt Spectrometer (EVS) [4] is shown in Figure 1. There are six banks of detectors covering angles in the range 35° to 53°, 57° to 76° and 125° to 137°, arranged symmetrically around the incident-beam direction. The forward-scattering banks are used primarily for studies of hydrogenous materials, for which back-scattering does not occur, whereas the back-scattering detectors provide the best resolution and highest energy transfers for heavier materials. ^{3}He gas detectors, linked to discriminators, measure the time of flight (TOF) from the moderator to the detector.

The final energy of the detected neutrons is fixed by a resonant foil technique. Gold or uranium foils, which have resonances at 4922 meV and 6671 meV, respectively, are placed in the scattered beam. The foils absorb neutrons with energies centred around the resonance energies. Gold foils are suitable for the study of hydrogenous and low-mass systems, where they give a resolution width that is typically 20% of the width of $J(y)$. The resonance at 4922 meV is well separated from the next resonance (60.3 eV), thus reducing the likelihood of "overlap effects" owing to two final neutron energies. Uranium foils are better for systems of high mass, since resolution in momentum space deteriorates with increasing mass of the scatterer [5].

Two measurements are made; one with the resonant foils in and one with the resonant foils out of the scattered beam. The foils are moved in and out of the scattered neutron beam every five minutes automatically. This is necessary in order to minimise systematic errors resulting from a time variation in the detector efficiencies. The difference between the two measurements defines a resolution function $R(E_1)=1-T(E_1)$ for the energy analysis of the scattered beam, where $T(E_1)$ is the foil transmisson.

3. Determination of $J(y)$ from EVS Data

Figure 2 is a schematic diagram of an inverse-geometry spectrometer. The energy E_1 and therefore velocity V_1 of the detected neutrons is fixed by the analyser foil. The velocity V_0 and energy E_0 of the incident neutron can be determined from the measured time of flight t,

$$t = \frac{L_0}{V_0} + \frac{L_1}{V_1} + t_0 , \tag{5}$$

where L_0 is the primary flight path from moderator to sample, L_1 the secondary flight path from sample to detector, and t_0 the delay time in measuring t. The

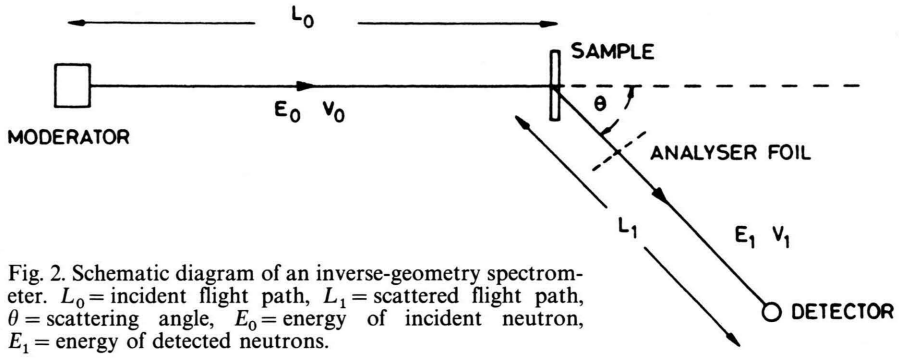

Fig. 2. Schematic diagram of an inverse-geometry spectrometer. L_0 = incident flight path, L_1 = scattered flight path, θ = scattering angle, E_0 = energy of incident neutron, E_1 = energy of detected neutrons.

energy transferred from the neutron to the target is

$$\omega = E_0 - E_1 , \tag{6}$$

and the momentum transfer q is given by

$$q = (k_0^2 + k_1^2 - 2k_0 k_1 \cos\theta)^{1/2}, \tag{7}$$

where θ is the scattering angle.

The values of q and ω defined by (5)–(7) uniquely relate y to a point in the TOF spectrum. They are easily calculated via the above equations once L_0, L_1, θ, t_0 and E_1 have been calibrated.

We now need to relate the counts $C(t)$ observed in a time bin to $J(y)$. The number of counts collected in a time channel of width Δt centred at t is [6]

$$C(t)\,\Delta t = I(E_0)\frac{dE_0}{dt}\Delta t \cdot N \frac{d^2\sigma}{d\Omega\, dE_1}\eta(E_1)\,\Delta\Omega\,\Delta E_1 , \tag{8}$$

where $I(E_0)\dfrac{dE}{dt}\Delta t$ is the number of incident neutrons/cm^2 corresponding to the time channel, N is the number of scattering atoms, $\Delta\Omega$ the detector solid angle, ΔE_1 the energy resolution of the analyser, $\eta(E_1)$ the efficiency of the detector, and $d^2\sigma/d\Omega\, dE_1$ is the partial differential neutron scattering cross-section. The latter quantity is related to the neutron scattering function $S(\boldsymbol{q}, \omega)$ via [3]

$$\frac{d^2\sigma}{d\Omega\, dE_1} = \frac{\sigma}{4\pi}\frac{k_1}{k_0} S(\boldsymbol{q}, \omega) . \tag{9}$$

From (2), (8), and (9) we obtain

$$C(t)\,dt = \left[\frac{N\,\Delta\Omega\,\eta(E_1)\,k_1\,\Delta E_1\,\sigma\,M}{4\pi}\right]\left(\frac{I(E_0)\dfrac{dE_0}{dt}\,dt\,J(y)}{k_0 q}\right). \tag{10}$$

The bracket [ ] contains all factors that are independent of t. It can be shown that $I(E_0) \propto E^{-0.9}$. Furthermore $k_0 \propto E_0^{0.5}$, and it is easily shown that for a fixed final energy E_1, $dE_0/dt \propto E_0^{1.5}$. Thus

$$J(y) = A\frac{qC(t)}{E_0^{0.1}}, \tag{11}$$

where A is the product of all parameters that are independent of t. The value of A can be determined from

$$\int J(y)\,dy = 1 , \tag{12}$$

which is necessary since $J(y)$ is a probability distribution.

3.1. *Instrument Resolution*

A clear understanding of the instrument resolution is essential for the interpretation of the data. The resolution of the instrument is determined primarily by the width of the resonance of the analyser foil. As a consequence of y-scaling (the phenomenon that $S(\boldsymbol{q}, \omega)$ scales with y through (2) and (3)), the resolution width in momentum space (y-space) is a function of the mass of the target particles. The contribution from E_1 is Lorentzian whereas the other contributions are Gaussian. Analytical expressions for the components of the instrument resolution have been dealt with in [5]. The five independent contributions to the resolution in y-space and the way in which each is determined are outlined below.

1. The energy width ΔE_1 of the resonant absorber. With a gold foil this is always the dominant contribution. The component of the resolution owing to the analyser foil was determined by scattering from samples with a high atomic mass (Pb, V, Sn). The Full Width at Half-Maximum (FWHM) of the Gaussian momentum distribution for high masses is small in comparison to the FWHM of the empirically

Lorentzian resolution function. A Voigt function (a convolution of a Lorentzian and a Gaussian) is fitted to the data. The FWHM of the Gaussian contribution is the square root of the sum of the squares of all Gaussian components; these can all be measured or calculated. Hence, by fitting a Voigt function with known Gaussian component and variable Lorentzian component, the Lorentzian resolution function for each detector is determined. The resultant widths agree closely with the values expected for the energy resolution in the case of gold and uranium foils.

2. The angular-resolution contribution is small except for scattering from hydrogenous systems. It was determined from the peak shape of powder diffraction peaks.

3. There is a distribution of L_0 values caused essentially by the depth of the neutron moderator. This contribution is always small compared to that from ΔE_1, determined by a Monte Carlo calculation.

4. There is a distribution of L_1 values owing to the finite sample width and detector depth, which must be calculated [4].

5. The uncertainty in the TOF owing to the finite width of the time bins, Δt. We choose Δt so that this effect is negligible.

4. Data Analysis

The data analysis procedure is outlined below for samples in which there is no preferred direction. At present the analysis is restricted to determining the mean kinetic energy. The assumption is that $J(y)$ is Gaussian.

The difference between the "foil-in" and "foil-out" spectra is determined for each scattering angle. In Fig. 3 we show the time-of-flight spectrum collected on detector 11 with the foil out of the scattered beam, for zirconium hydride, together with a time-of-flight spectrum measured with the foil in. The difference spectrum yields those neutrons captured by the foil. Figure 4 shows a series of time-of-flight spectra for one of the low-angle banks. Note how the separation of recoil peak and nearly elastic scattering increases with angle.

The data are then transformed to y-space according to (2). The near-elastic scattering owing to the sample-holder and atoms other than hydrogen is subtracted by fitting a Lorentzian to this part of the spectrum.

The calculation of the atomic kinetic energy assumes that the measured $J(y)$ is a Voigt function with

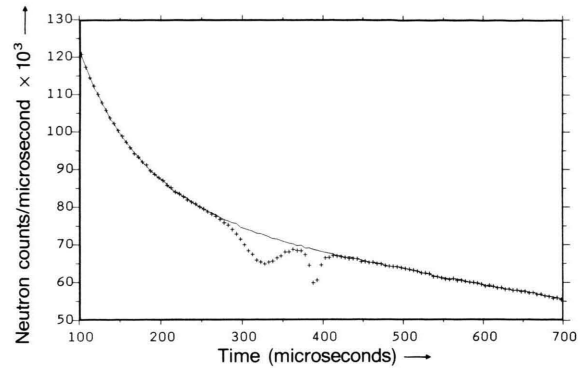

Fig. 3. "Foil in" (crosses) and "foil out" (line) time-of-flight spectra for ZrH_2 measured on detector 11.

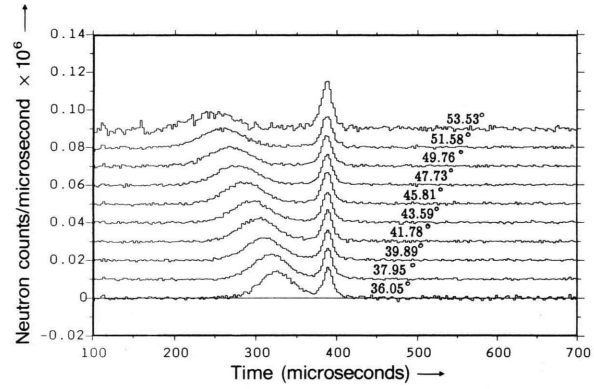

Fig. 4. A series of "foil in" in "foil out" time-of-flight difference spectra. The broad peak is due to hydrogen scattering and the narrow peak is due to sample-holder (aluminium) scattering.

a fixed Lorentzian resolution component, whose width is determined as explained in the previous section. The width of the Gaussian component is extracted, and a mean value calculated from the results for each detector. The justification for fitting a Voigt function is that the resolution function is empirically well described by a Lorentzian function in momentum space and that for the majority of materials measured on EVS, anharmonicities are negligible, implying that the momentum distribution is Gaussian. Theoretical calculations of $n(\boldsymbol{p})$ for a harmonic oscillator with small x^4-perturbations were undertaken. Using values for the perturbations calculated by Ikeda et al. for a series of metal hydrides [7], it was shown that any deviations from Gaussian behaviour are negligible.

The resolution function in y-space is a function of the scattering angle. In the case of zirconium hydride, the resolution FWHM varies from 1 to 2 $Å^{-1}$ over an angular range from 35 to 53 degrees. It is important to correct for this. There are two methods used for obtaining a single data set representative of all the detectors. Firstly, a program was written to transform the data sets for all detectors to a common resolution function. This works on the principle that the convolution of two Lorentzians yields a Lorentzian whose FWHM is the sum of the two. The alternative is to sum all data sets and deconvolute with a composite resolution function. The advantage of the latter method is that it makes no assumptions about the resolution function; on the contrary – it is necessary to determine the composite resolution function experimentally. This has been achieved.

5. Examples of Measurements

5.1. Zirconium Hydride at 290 K

Two measurements of the momentum distribution of hydrogen in ZrH_2 at 290 K are detailed below. Figure 5 shows the two measurements superimposed. The broadening owing to the instrument resolution has not been removed and should be the same in each case. Table 1 shows the results of the data analysis procedures described in the previous section for each run.

The FWHM of $J(y)$ is σ_a for the low-angle bank and σ_b for the high-angle bank. The relationship between the kinetic energy of a particle in a harmonic potential and the FWHM of $J(y)$ is given by

$$E = \frac{\hbar^2}{2M}\sigma^2 . \tag{13}$$

The FWHM for both banks is given by σ_c. The result for both banks after symmetrisation about $y = 0$ is given by σ_s. The results are consistent with one another. Furthermore, symmetrisation has only a small effect on the FWHM, implying that the data were closely symmetrical before symmetrisation. This is additional evidence that the IA is well satisfied.

Figure 6 shows the measured Compton profile in ZrH_2 at 290 K determined from several zirconium hydride runs. The experimental points (o) are fitted to a convolution of the resolution function (narrow peak) with a Gaussian (line). The fit gave an rms momentum

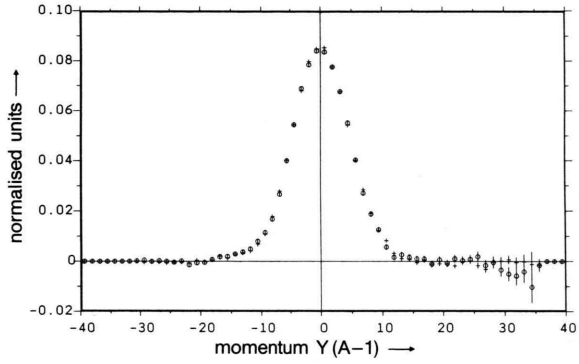

Fig. 5. Measured $J(y)$ for two ZrH_2 runs (see Table 1). Run 1113 (crosses), run 1121 (circles).

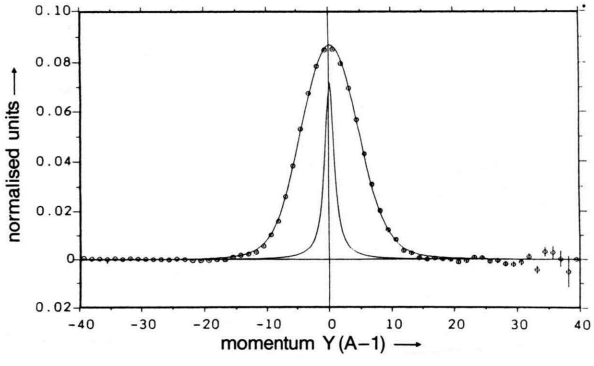

Fig. 6. The measured Compton profile of ZrH_2 at 290 K. The experimental points (o) are fitted to a convolution of the resolution function (narrow peak) with a Gaussian (line).

Table 1. The FWHM of $J(y)$ is given below for the low-angle bank of detectors (σ_a), the high-angle bank (σ_b) and both banks at forward scattering (σ_c). σ_s is the value determined from the symmetrised data. M is the mass of the proton and C the intercept determined by fitting the positions of the maxima in $J(y)$ measured on individual detectors. These samples were measured at room temperature.

Run	σ_a ($Å^{-1}$)	σ_b ($Å^{-1}$)	σ_c ($Å^{-1}$)	σ_s ($Å^{-1}$)	M (amu)	C (meV)
1113	4.16 ± 0.02	4.13 ± 0.06	4.15 ± 0.03	4.18 ± 0.04	1.0034 ± 0.0051	-36 ± 27
1121	4.19 ± 0.04	4.17 ± 0.08	4.18 ± 0.04	4.17 ± 0.04	1.0062 ± 0.0035	-30 ± 19

Sample	Temp. (K)	σ (Å^{-1})	σ_s (Å^{-1})	M (amu)	C (meV)
ZrH_2	290	4.16 ± 0.01	4.17 ± 0.01	1.0068 ± 0.0005	-40 ± 27
ZrH_2	20	4.20 ± 0.03	4.24 ± 0.04	1.0115 ± 0.0022	-55 ± 19
NbH	290	4.33 ± 0.03	4.31 ± 0.03	1.010 ± 0.011	-40 ± 50
NbH	20	4.44 ± 0.06	4.43 ± 0.04	1.014 ± 0.007	-14 ± 34
TiH_2	290	4.29 ± 0.04	4.28 ± 0.04	1.008 ± 0.009	-34 ± 43
TiH_2	20	4.34 ± 0.04	4.29 ± 0.04	0.998 ± 0.014	-80 ± 64
CaH_2	290	3.80 ± 0.03	3.77 ± 0.04	1.007 ± 0.004	-38 ± 22
CaH_2	20	3.70 ± 0.03	3.66 ± 0.03	1.007 ± 0.003	-35 ± 17

Table 2. σ is the FWHM of $J(y)$ measured on the low-angle bank of detectors, and σ_s is determined from the symmetrised data. M is the mass of the proton and C the intercept determined by fitting the positions of the maxima in $J(y)$ measured on individual detectors.

Element	T (K)	Θ_D (K)	M (amu)	M_{exp} (amu)	$\langle p \rangle$ (Å^{-1})	σ (Å^{-1})
Lithium	300	400	6.94	6.91 ± 0.06	6.83	6.89 ± 0.04
Beryllium	290	1000	9.012	8.99 ± 0.02	9.06	9.40 ± 0.07
Boron-11	290	1250	11.00	11.06 ± 0.07	10.80	10.86 ± 0.16
Carbon	290	1860	12.011	12.07 ± 0.05	13.32	11.74 ± 0.33
Aluminium	290	394	26.982	27.34 ± 0.39	13.26	13.04 ± 0.07

Table 3. M is the known mass of the scattering nucleus, and M_{exp} is the mass of the scattering nucleus determined from the positions of the recoil peaks. σ is the FWHM of $J(y)$ and $\langle p \rangle$ is the root-mean-square value of the momentum $\boldsymbol{p}$ of the particle lying along the scattering vector, calculated using the Debye model. Θ_D is the Debye temperature, and the temperature is T.

of 4.16 ± 0.02 Å^{-1} and is consistent with a harmonic potential of fundamental frequency 144 ± 1 meV. This compares to values between 140 and 170 meV from measurements of transition energies by neutron spectroscopy. Similar data were obtained for the other hydride samples.

5.2. *Metal Hydrides at 20 K and 290 K*

The momentum distributions of four metal hydrides were measured on EVS at 20 K and 290 K. The samples were obtained commercially and no information as to the hydrogen concentration or the presence of multiple phases was available from the supplier.

In Table 2 we give the rms momentum (σ) for 4 different hydrides at 290 K and 20 K. Within statistical error, no difference can be detected between the distributions at the two temperatures. Note that the fitted intercept parameter C is negative (see Table 2). This is in agreement with exact simulations of the data that have been performed.

5.3. *Lithium from 20 K to 290 K*

The momentum distribution of lithium metal was measured on EVS and the FWHM σ compared to the Debye model as a function of temperature. Figure 7 shows the data for lithium measured on the back-scattering bank at 22.6 K (line) and 260.5 K (stars). Each data set is a sum of the data collected from each of the ten detectors in this bank. The resolution broadening is the same in each case, therefore the width difference of the two data sets is due to temperature. Note that the base line for each data set is zero out to high momenta, demonstrating the high quality of the data.

The relationship between σ and T in the isotropic Debye approximation is given by [8]

$$\sigma = (MT^*)^{1/2} \tag{14}$$

and

$$T^* = \frac{1}{3} \int \omega Z(\omega) \coth\left(\frac{\omega}{T}\right) d\omega , \tag{15}$$

where $Z(\omega)$ is the Debye density of states. Figure 8 shows a plot of σ against temperature for detectors in the range 125° to 137° (circles) and 57° to 76° (crosses). The line is the theoretical calculation of σ in the Debye approximation. In contrast to previous studies [9], we find that the harmonic Debye model gives a good fit to the data.

Lithium possesses a martensitic transition [10] at 78 K where it transforms from a bcc structure into a close-packed rhombohedral phase. The increase in density at this transition has been calculated to be 1.2%. Owing to the smaller average atomic spacing, it is reasonable to expect a corresponding narrowing in the spatial potential that each lithium atom "sees"

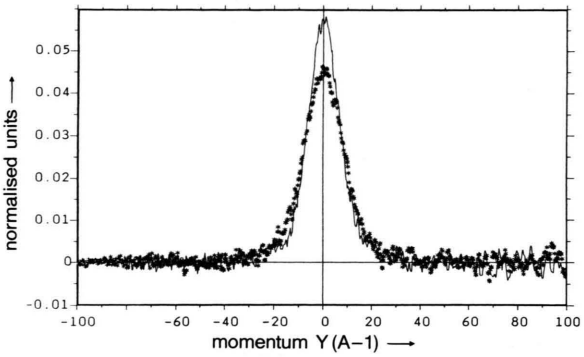

Fig. 7. Measured Compton profile on the back-scattering bank at 22.6 K (line) and 260.5 K (stars). Each data set is a sum of the data collected from each of the detectors in the bank.

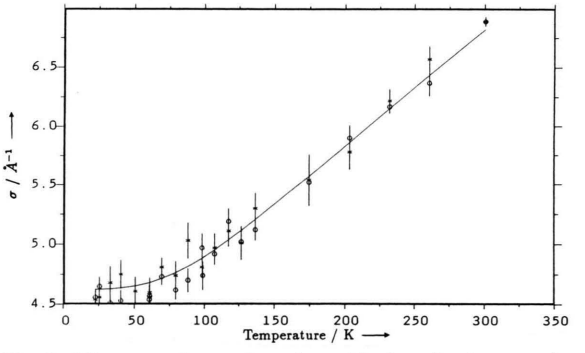

Fig. 8. The experimental points (circles: back-scattering bank, crosses: 57°–76° bank) show σ as a function of temper ature in lithium metal. The line is the theoretical calculation of σ in the Debye approximation.

and, consequently, a broadening of $J(y)$. A 1.2% change in volume corresponds to a 0.4% change in one dimension. Assuming that lithium atoms move on average 0.4% closer to each other at the transition, and assuming a harmonic potential, it is expected that the kinetic energy of each lithium atom is increased on average by 0.8%. The margin of error in EVS measurements of the kinetic energy is around 1%. Consequently, the effect was not observed owing to the limited statistical accuracy of the data.

5.4. The Elements Li, Be, ^{11}B, C and Al

The atomic Compton profiles of natural Li, Be, C, Al, and ^{11}B were measured. Gold analyser foils were used, being suitable for these low-mass systems. The kinetic energies thus obtained were compared to the Debye model for the solids in question. The results tabulated in Table 3 show the calculated σ determined from one or more runs in the case of each element. The agreement is reasonable, remembering that for systems of these masses, the resolution is not as good as in the case of scattering from hydrogenous systems. There is a discrepancy between σ and $\langle p \rangle$ in the case of carbon. This is explained by the fact that the sample was pyrolytic graphite. The Debye temperature quoted is for polycrystalline graphite. The sample was oriented so that σ was measured approximately perpendicular to the plane of the carbon layers. The value for σ is smaller therefore, because the bonding is weaker in this direction.

M is the atomic mass, M_{exp} the atomic mass determined from the positions of the recoil peaks and $\langle p \rangle$ is the root-mean-square atomic momentum determined from the Debye model. In each case, σ is determined from the back-scattering bank, which offers the highest resolution. The determined masses all agree well with the known values. The errors tend to be underestimated if the measured data do not fit well to a Voigt function. This may occur if there are complications in data analysis. For example, the sample-can scattering may occur near the recoil peak if the atomic masses of the sample and sample container are close.

5.5. Recent Measurements Performed on EVS

Recent measurementss include water, heavy water, a single crystal of potassium hydrogen carbonate (a system with aligned hydrogen bonds), a stretched polymer (exhibiting anisotropy along the stretching direction) and a study of the difference in the momentum distributions of liquid ^4He above and below the superfluid transition temperature.

We have summarised the present state of development of neutron Compton scattering on the EVS spectrometer at ISIS. The data so far collected demonstrate the potential of the EVS instrument for obtaining fundamental information on atomic dynamics. EVS is a spectrometer with a wide range of applications in many different fields of research.

Acknowledgement

The authors are indebted to the Science and Engineering Research Council for the funding of this work.

[1] B. Williams, Compton Scatttering, McGraw-Hill, New York 1977.
[2] P. C. Hohenberg and P. M. Platzmann, Phys. Rev. **152,** 198 (1966).
[3] S. W. Lovesey, Theory of Neutron Scattering from Condensed Matter, Oxford University Press, London 1987, Vol. 1.
[4] J. Mayers and A. C. Evans, Measurement of Atomic Momentum Distribution Functions by Neutron Compton Scattering. Progress on the EVS Spectrometer during 1990. Rutherford Appleton Laboratory Report, RAL-91-048 (1991).
[5] C. Andreani, G. Baciocco, R. S. Holt, and J. Mayers, Nucl. Inst. Methods **A 276,** 297 (1989).
[6] C. G. Windsor, Pulsed Neutron Scattering, Taylor and Francis, London 1981.
[7] S. Ikeda and N. Watanabe, J. Phys. Soc. Japan **56,** 565 (1986).
[8] J. Mayers, C. Andreani, and G. Baciocco, Phys. Rev. B **39,** 2022 (1989).
[9] M. P. Paoli, D. Phil. Thesis, Oxford University 1988.
[10] Y. R. Wang and A. W. Overhauser, Phys. Rev. B **34,** 8401 (1986).